A platform for x-ray Thomson scattering measurements of radiation hydrodynamics experiments on the NIF[a)]

H. J. LeFevre,[1, b)] K. Ma,[2] P. X. Belancourt,[3] M. J. MacDonald,[4] T. Döppner,[4] C. M. Huntington,[4] E. Johnsen,[2] P. A. Keiter,[5] and C. C. Kuranz[5]

[1)] *Applied Physics, 450 Church Street, University of Michigan Ann Arbor, MI 48109, USA*

[2)] *Mechanical Engineering, 2350 Hayward Street, University of Michigan Ann Arbor, MI 48109, USA*

[3)] *Climate and Space Sciences and Engineering, 2455 Hayward Street, University of Michigan Ann Arbor, MI 48109 USA*

[4)] *Lawrence Livermore National Laboratory Livermore, 7000 East Avenue, CA 94550, USA*

[5)] *Climate and Space Sciences and Engineering, 2455 Hayward Street, University of Michigan Ann Arbor, MI 48109, USA*

(Dated: 8 August 2018)

We present an experimental design for a radiation hydrodynamics experiment at the National Ignition Facility that measures the electron temperature of a shocked region using the x-ray Thomson scattering technique. Previous National Ignition Facility experiments indicate a reduction in Rayleigh-Taylor instability growth due high energy fluxes, compared to the shocked energy flux, from radiation and electron heat conduction. In order to better quantify the effects of these energy fluxes, we modified the previous experiment to allow for non-collective x-ray Thomson scattering to measure the electron temperature. Photometric calculations combined with synthetic scattering spectra demonstrate an estimated noise.

I. INTRODUCTION

High-energy-density (HED) hydrodynamics experiments allow for the study of a wide range of physics, from basic hydrodynamics[1,2] to instability growth in young supernova remnants[3]. At the National Ignition Facility (NIF) at Lawrence Livermore National Laboratory 1.8 MJ of UV laser light in 192 beams irradiates a mm-scale hohlraum to "drive" these hydrodynamic systems in the HED regime[4,5]. Each NIF beam is an independent beamline and delivers about 2 TW of 3ω laser power to the target[4,5]. Previous experiments used the x-ray radiography technique to image the evolution of hydrodynamic instabilities.[1–3]. The experiment of interest here[3], referred to as Kuranz experiment from here on, used a shock tube, which contains a plastic component and a low-density foam, attached to a "half-hohlraum", which generates an x-ray bath when irradiated with the NIF laser beams. The hot environment inside the hohlraum ablates the plastic target material, increasing the pressure and launching a shock into the shock tube. The shock crosses the plastic-foam interface, which includes precision-machined perturbations that will grow due to the Rayleigh-Taylor (RT) instability.

Kuranz *et al.* found that the RT growth was reduced when energy fluxes were large compared to the shocked material energy flux, ρu_s^3 where ρ is the unshocked material density and u_s is the shock velocity. Energy fluxes, including fluxes from both radiation and electron heat conduction, were varied by changing the laser energy. The Kuranz experiments were performed in either the high-energy-flux regime or, for comparison, the low-energy-flux regime (further details can be found in Kuranz *et. al.*). In order to better quantify the effects of these energy fluxes we have designed experiments to measure the electron temperature of the shocked region using x-ray Thomson scattering (XRTS).

Previous experiments on the NIF fielded XRTS to characterize the high-density plasma in indirectly driven, spherical implosions[6–8]. This experiment deployed the MACS spectrometer, which uses a cylindrically curved highly oriented pyrolytic graphite (HOPG) crystal and a four strip MCP detector with a 100 or 230 ps gate duration[9,10]. Effective shielding is key to XRTS experiments due to typically low scattered signal. We plan to modify the shielding scheme used in previous XRTS NIF experiments[6].

II. X-RAY THOMSON SCATTERING

XRTS is a measurement technique that uses x-rays to probe a scattering volume and interact with free electrons, tightly bound electrons, and bound to free electrons. X-rays that scatter off of the free electrons are sensitive to electron temperature. These x-rays, based on geometry, can interact with either individual electrons bound to ions and free electrons in the non-collective regime or the electron plasma waves and ion acoustic waves excited in the plasma in the collective regime. The

[a)] Contributed paper published as part of the Proceedings of the 22nd Topical Conference on High-Temperature Plasma Diagnostics, San Diego, California, April, 2018.

[b)] hjlefe@umich.edu

electron structure factor

$$S_{ee}(k,\omega) = |f_I(k) + q(k)|^2 S_{ii}(k,\omega) + Z_f S^0_{ee}(k,\omega) + Z_b \int d\omega' \tilde{S_{ce}}(k,\omega-\omega') S_S(k,\omega'), \quad (1)$$

describes the interactions, where the first term describes the scattering off of electrons bound to ions, the second term describes free electron photon interactions, and the third term describes bound-free interactions[11,12]. In Eq. 1, Z_f and Z_b are the free and bound electrons per nucleus, with Z_f also containing the valence electrons. In the first term, $f_I(k)$ represents the scattering off of tightly bound electrons and $g(k)$ scattering off of valence electrons. The XRTS technique in the non-collective regime is sensitive to electron temperature and effective ionization[11].

III. TARGET GEOMETRY

The target package is the same as the one used in the Kuranz experiments[3], but without a perturbed interface. This will act as a simple case to test the platform before increasing the complexity with instability growth. The tube will be 1.39 mm in inner diameter driven by a hohlraum with an open end, sometimes called a "halfraum". The x-ray bath generated in the halfraum irradiates a 150 μm thick, 1.4 g cm^{-3} plastic ablator followed by a 11 μm Au thermal shield. A gold tamper provides structural support around the side of the shock tube closest to the halfraum. Fig. 1a shows this target structure.

Eight NIF beams irradiate a Zn foil, mounted 2 mm from the tube wall to generate the x-ray probe. When the NIF beams irradiate the Zn foil a plasma is formed and heated, which produces 9 keV Zn He-α emission that passes through a collimator to limit the divergence of probe x-rays. The Au collimator is 1 mm long and 280 μm in inner diameter. The foil standoff distance is 1 mm from the collimator entrance, making the beam divergence $\frac{\theta}{2} = 19.4^o$ and the beam diameter about 800 μm at the center of the tube. Increasing the collimator inner diameter or decreasing the length can improve the scattering signal strength at the expense of additional measurement error.

The intersection of the probe beam and the field of view of the crystal, inside the target, defines the scattering volume. The MACS geometry sets the crystal field-of-view, with the diagnostic axis aligned to polar angle 90^o and azimuth 78^o, where polar angle 0^o and azimuth 0^0 is the top of the chamber. A window in the tube, directed to account for the 10^o crystal offset in the MACS[9], is 110^o from the probe beam to define the scattering volume and the scattering angle, as shown in Fig. 2. The window is 215 μm in the crystal dispersion direction perpendicular to the shock propagation and 200 μm parallel to the shock propagation. Lengthening the window in the crystal dispersion direction will allow for more scattering signal to be collected at the expense of a well-defined scattering angle.

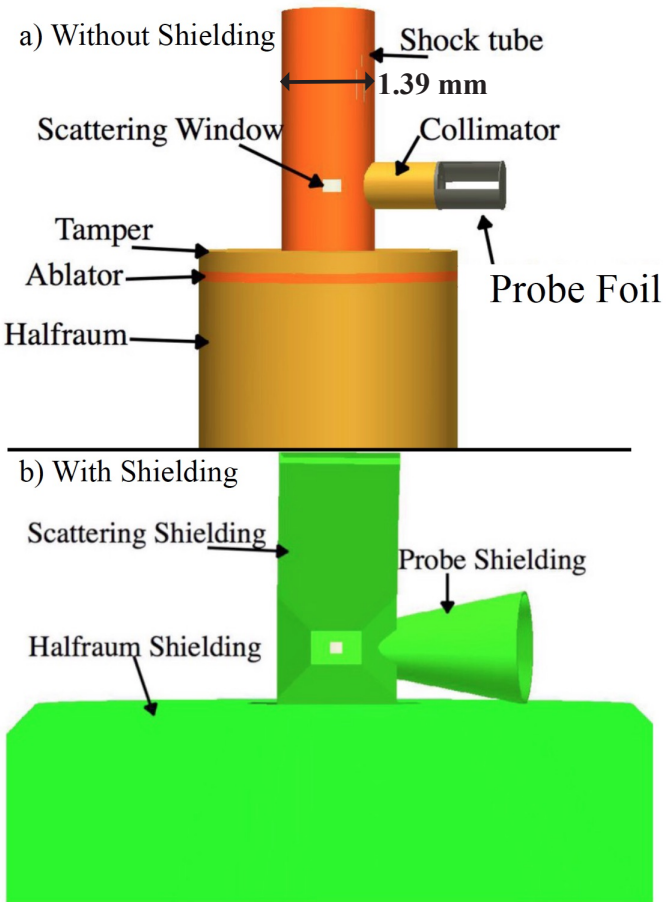

FIG. 1. a) The XRTS target design, from the MACS axis view, showing the shock tube, probe source and collimator with labels indicating the target structure. The collimator, halfraum, and tamper are made of gold. The shock tube and ablator are plastic. The backlighter foil is Zn. b) The XRTS target from the MACS axis view showing that the shielding completely obscures the diagnostic from the non-scattering target emission. All three labeled shielding components are made of high-Z material.

Due to the generally low signal produced in XRTS, shielding, shown in Fig. 1 b, is necessary to block the non-scattered emission from reaching the detector during the measurement gate time. A "skirt" at an angle of 45^o with a length of 5.5 mm and an offset of 3 mm from the edge of the halfraum shields the detector from the halfraum emission. A cone that is 2.5 mm tall with a cone angle of 11^o shields the detector from the Zn probe foil emission. An angled shield that extends the length and width of the shock tube shields the detector from the self emission of the shock heated material.

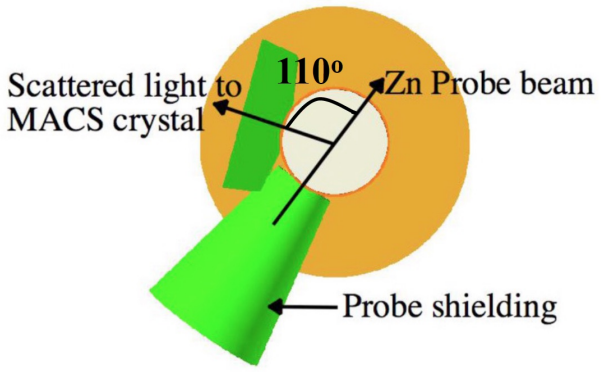

FIG. 2. The scattering geometry of the target. The scattering window is centered 110^o from the probe beam but due to the geometry of MACS crystal within the diagnostic it is pointed at polar angle 90^o azimuth 68^o, 10^o from the diagnostic axis.

IV. RADIATION HYDRODYNAMICS SIMULATIONS

Radiation hydrodynamics simulations were performed using the CRASH code, a multidimensional Eulerian code with dynamic adaptive mesh refinement, multigroup-diffusion radiation transport, flux-limited electron heat conduction and tabular equations of state[13]. The experiment was simulated using a hohlraum radiation temperature profile calibrated using the experimental conditions to match the data from Kuranz *et. al.* Simulations of the experiment using the CRASH code explored materials that could provide the desired physics while also allowing for simple interpretation of the XRTS data.

Figure 3 shows simulation results of mass density and electron temperature of the high-energy flux (Fig. 3a) and low-energy flux (Fig. 3b) conditions at the distance of the diagnostic window. In both Figure 3a and 3b there is an increase in mass density indicating a shock in the foam material. The plastic-foam interface trails the shock front. In Figure 3a, there is an increase in heating upstream of the shock and at the material interface due to the high-energy fluxes in the system.

These simulation results used a 30 mg/cc CRF foam, however, the Kuranz *et. al.* experiments used 20 mg/cc SiO_2 foam. CRF foam is preferable due to its simple chemical composition (dominantly C) so that multi-species effects will be relatively unimportant in the XRTS measurement, compared to SiO_2. In addition, C is lower Z than Si or O, which also reduces the complexity of the analysis. Scattering spectra depend on the ionization, electron temperature, and ion temperature. Every additional species increases the number of correlations between various scatterers in the data, complicating the analysis. A density of 30 mg/cc is the current limit of production capabilities for CRF foam. Switching materials will result in a simplified interpretation of the XRTS data, while the key dynamics of the experiment remain the same.

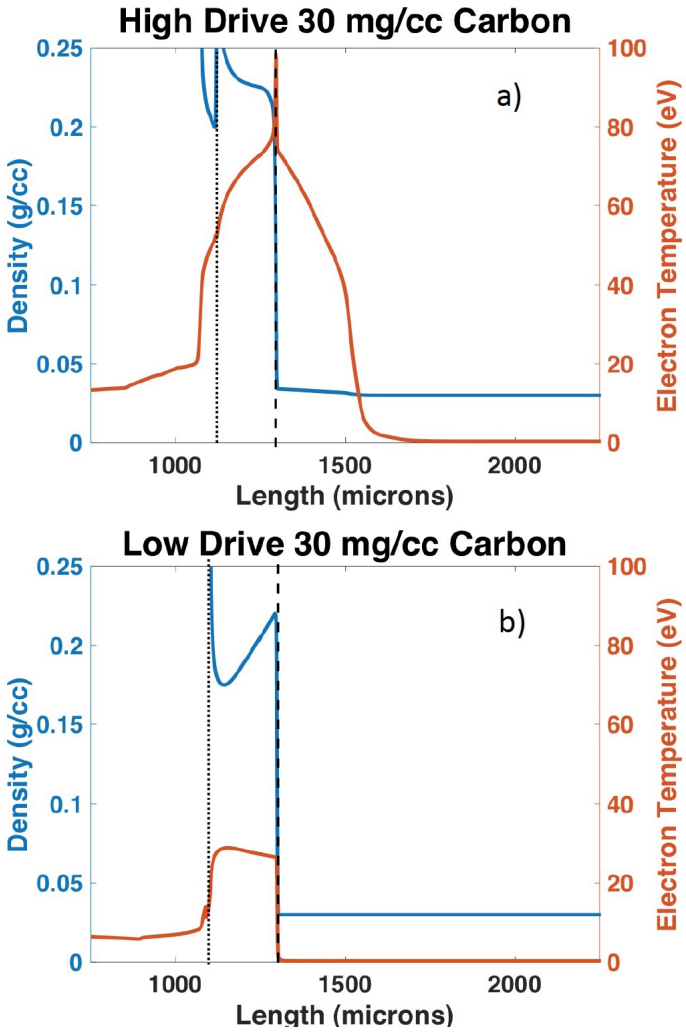

FIG. 3. a) CRASH simulation showing the high drive shock having propagated to the center of the scattering window. There is a clear precursor and Zel'Dovich spike indicating that it is a radiative shock. b) CRASH simulation showing the low drive shock having propagated to the center of the scattering window.

V. XRTS PHOTOMETRICS

To test if the measurement is possible, the number of photons reaching the detector is estimated for the high-energy flux and low-energy flux cases. Since the scattering will be in the non-collective regime, the number of the photons in the inelastic peak can be estimated[11] by,

$$N_\gamma = \left(\frac{E_l}{E_p}\eta_x\right)\left(\frac{n_e\sigma_{Th}l}{(1+\alpha)^2}\right)\left(\frac{\Omega_c}{4\pi}\tau_c\eta_a\right)\left(\frac{\Omega_d}{4\pi}QE\right)\eta_f, \quad (2)$$

Parameter	Value	Parameter	Value
E_p	9000 eV	E_l	4050 J
η_x	0.01	α	0.31
σ_{th}	$6.55 * 10^{-25}$ cm^2	l	215 μm
Ω_c	0.0679	τ_c	0.131
η_a	0.92	Ω_d	0.00028 str
QE	0.05	R_{int}	3 mrad
η_f	0.69		

TABLE I. The parameters used in the photometric calculation, where E_l is the laser energy during the 230 ps MCP gate time, E_p is the Zn He-α photon energy, η_x is the x-ray conversion efficiency[14], n_e is the electron density, σ_{Th} the Thomson scattering cross section, l is the plasma scale length, α is the scattering parameter, τ_c is the collimator throughput, η_a is the attenuation through the target, Ω_d is the detector solid angle, QE is the detector quantum efficiency[11], and η_f is the attenuation through the MACS blast shield

The collimator throughput is the fraction of emitted intensity from the Zn foil that propagates through the collimator modeled as a collection of point sources of equal intensity. The values used to evaluate this equation are given in Table I, where R_{int} is the integrated reflectivity of the MACS HOPG crystal used to calculate Ω_d. Ω_d is the integrated reflectivity times the acceptance angle in the non-dispersive direction, $\Omega_d = \frac{24}{250} * R_{int}$, where 24 mm is the effective width of the crystal and 250 mm is the distance from the target to the crystal. Using $n_e = 2.2 * 10^{22}$ cm^{-3} for the low-energy flux case and $n_e = 3.5 * 10^{22}$ cm^{-3} for the high-energy flux case, the calculated number of photons in the inelastic peak are 8000 and 5000 for the high-energy flux and low-energy flux cases respectively.

VI. SYNTHETIC SCATTERING SPECTRA AND ESTIMATED NOISE

Synthetic spectra were calculated for the high-energy flux and low-energy flux cases, using the simulation output in Fig. 3, with the X-Ray Scattering (XRS) code[12]. The XRS code calculates the electron structure factor for a particular scattering angle and probe energy for a set of plasma parameters: number density, mass density, ionization, electron temperature, and ion temperature. It has the ability to use several models for the bound-free and the bound-bound scattering with the option of convolving the calculated spectrum with a probe spectrum to account for structure in the source. For the low-energy flux case, the calculation parameters were: electron temperature of 20 eV, ionization of 2.3, electron density of 2.2×10^{22} cm^{-3}, mass density of 0.21 g cm^{-3}, and for the high-energy flux case: electron temperature of 70 eV, ionization of 3.2, electron density of 3.5×10^{22} cm^{-3}, mass density of 0.21 g cm^{-3}. The ions and electrons were assumed to be in equilibrium and the scattering was calculated using the random phase approximation for the free-free scattering, which states that the electron motion is mostly random and interparticle interactions average to zero[15]. Figs. 4 a and b show the plotted spectra as convolutions of the calculated spectra and a Gaussian with a width selected to match published MACS data[7]. This convolution accounts for broadening due to the measurement geometry, detector electronics, and plasma conditions. However, this is likely an overestimate of the broadening for our geometry due to their

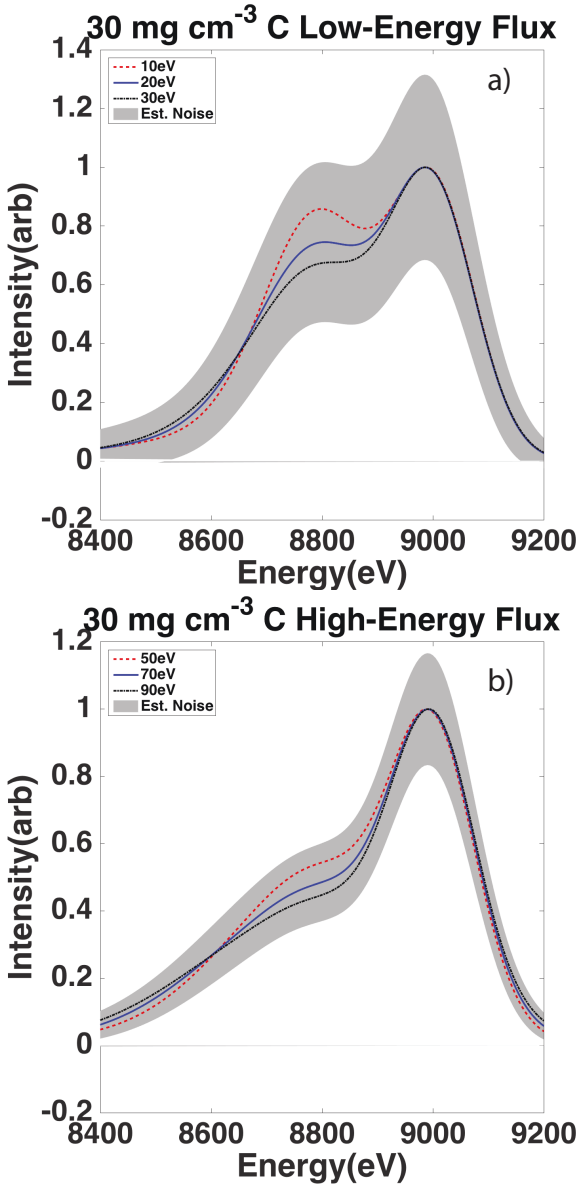

FIG. 4. a) Low drive synthetic spectra with estimated detector noise and center spectra at the simulated value of 20 eV including two additional spectra at ± 10 eV to show temperature sensitivity. b) High drive synthetic spectra with estimated detector noise and center spectra at the simulated value of 70 eV including two additional spectra at ± 20 eV to show temperature sensitivity.

exit aperture being an order of magnitude larger in the crystal dispersion direction.

To understand the feasibility of making a significant measurement with the data collected during an experiment, the calculated spectra shown in Figs. 4 a and 4 b include estimated counting noise. Separating the synthetic spectra into the bound-bound, bound-free, and free-free terms, then using the photometric calculation to convert the free-free component from arbitrary intensity to photon count produces an estimate of the photon count spectrum. The noise in the signal is then $\pm\sqrt{N}$ since the photons follow a Poisson distribution and the detector noise is dominated by Shot noise[16]. However, MCPs are non-ideal amplifiers so there is a multiplicative noise factor used to account for this[16]. When considering the noise factor as the input power signal to noise ratio(SNR) to the output power SNR, this value is about 2.5-3[16–18]. Here the noise factor is taken to be 2.5, resulting in a reduction of $\frac{1}{2.5} = 0.4$ to the SNR[16]. A more detailed calculation of the detector noise will be included in a future publication after the experiments. Figs. 4 a and 4 b show the synthetic spectra with a gray shaded region that represents estimated symmetric error bars, described above, at each point on the spectrum.

There are additional sources of measurement error, which have not been accounted for in the synthetic spectra. The simulations described above predict that the shock velocity is about 70 μm ns^{-1} for low-energy flux and about 120 μm ns^{-1} for the high-energy flux case. The gate time of the MACS MCP strips is either 100 or 230 ps, which means that the shock front travels around 20 μm during that time. The window is 200 μm in the direction of the shock propagation and the shocked region is about 300 μm in width, this suggests that motion blurring will not contribute significantly to the measurement uncertainty. However, depending on laser timing error, the window width may need to be increased to accommodate uncertainty in the probe lasers delay from the halfraum drive lasers. The synthetic spectra shown above are for a single scattering angle, but due to the finite window size and diverging probe beam multiple scattering angles reach the crystal, which are not currently accounted for. Figs. 3a and 3b show that gradients in the electron temperature and density are relevant on the scale of the scattering volume, which will affect the measurement. This means that the XRTS measurement is probing over many different states and that the electron temperature extracted will be the first moment in energy of the Maxwellian distribution instead of the temperature behind the front.

VII. CONCLUSION

The experimental design presented allows for the electron temperature to be extracted from radiation hydrodynamics experiments on the NIF using XRTS. Simulations demonstrated that 30 mg cm^{-3} CRF foam is a strong candidate for the target material that is able to generate high energy fluxes under these experimental conditions and is within current production capabilities. Scattering calculations show that the spectra are reasonably sensitive to temperature, and a noise estimation demonstrates that the counting noise should allow for a measurement.

ACKNOWLEDGMENTS

This work is funded by the NNSA-DS and SC-OFES Joint Program in High-Energy-Density Laboratory Plasmas, grant number DE-NA0002956 and the National Science Foundation through the Basic Plasma Science and Engineering program grant number 1707260. The work of T.D., C.H. and M. J. M. was done under the auspices of the U.S. Department of Energy by Lawrence Livermore National Laboratory under Contract No. DE-AC52-07NA27344. T.D. was supported by Laboratory Directed Research and Development (LDRD) Grant No. 18-ERD-033.

[1] S. R. Nagel *et al.*, Physics of Plasmas **24**, 072704 (2017).
[2] F. W. Doss, K. A. Flippo, and E. C. Merritt, Phys. Rev. E **94**, 023101 (2016).
[3] C. C. Kuranz *et al.*, Nature Communications **9**, 1564 (2018).
[4] G. H. Miller, E. I. Moses, and C. R. Wuest, Nuclear Fusion **44**, S228 (2004).
[5] E. I. Moses, R. N. Boyd, B. A. Remington, C. J. Keane, and R. Al-Ayat, Physics of Plasmas **16**, 041006 (2009).
[6] D. Kraus *et al.*, Journal of Physics: Conference Series **717**, 012067 (2016).
[7] D. Kraus *et al.*, Phys. Rev. E **94**, 011202 (2016).
[8] T. Döppner *et al.*, Journal of Physics: Conference Series **500**, 192019 (2014).
[9] T. Döppner *et al.*, Review of Scientific Instruments **85**, 11D617 (2014).
[10] T. Döppner *et al.*, Review of Scientific Instruments **87**, 11E515 (2016).
[11] S. H. Glenzer and R. Redmer, Rev. Mod. Phys. **81**, 1625 (2009).
[12] G. Gregori *et al.*, Physics of Plasmas **11**, 2754 (2004).
[13] B. van der Holst *et al.*, The Astrophysical Journal Supplement Series **194**, 23 (2011).
[14] M. A. Barrios *et al.*, Review of Scientific Instruments **85**, 11D502 (2014).
[15] D. Pines and D. Bohm, Phys. Rev. **85**, 338 (1952).
[16] K. G. McCammon, K. G. Hagans, and A. K. Hankla, "Noise performance of microchannel plate imaging systems," (1991).
[17] E. J. Gamboa, C. M. Huntington, E. C. Harding, and R. P. Drake, Review of Scientific Instruments **81**, 10E310 (2010).
[18] C. J. Pawley and A. V. Deniz, Review of Scientific Instruments **71**, 1286 (2000).